Geotextiles and Geomembranes 29 (2011) 1–16

Contents lists available at ScienceDirect

Geotextiles and Geomembranes

journal homepage: www.elsevier.com/locate/geotexmem

Reinforcement load and deformation mode of geosynthetic-reinforced soil walls subject to seismic loading during service life

Huabei Liu [a,*], Xiangyu Wang [b], Erxiang Song [b]

[a] Department of Civil Engineering, City College of New York/CUNY, 160 Convent Ave., New York, NY 10031, USA
[b] Department of Civil Engineering, Tsinghua University, Beijing 100084, China

ARTICLE INFO

Article history:
Received 31 May 2009
Received in revised form
12 April 2010
Accepted 12 June 2010
Available online 8 August 2010

Keywords:
Geosynthetic-reinforced-soil walls
Deformation mode
Reinforcement load
Seismic loading
Creep

ABSTRACT

A Finite Element procedure was used to investigate the reinforcement load and the deformation mode for geosynthetic-reinforced soil (GRS) walls subject to seismic loading during their service life, focusing on those with marginal backfill soils. Marginal backfill soils are hereby defined as filled materials containing cohesive fines with plasticity index (PI) >6, which may exhibit substantial creep under constant static loading before subjected to earthquake. It was found that under strong seismic loading reinforced soil walls with marginal backfills exhibited a distinctive "two-wedge" deformation mode. The surface of maximum reinforcement load was the combined effect of the internal potential failure surface and the outer surface that extended into the retained earth. In the range investigated, which is believed to cover general backfill soils and geosynthetic reinforcements, the creep rates of soils and reinforcements had small influence on the reinforcement load and the "two-wedge" deformation mode, but reinforcement stiffness played a critical role on these two responses of GRS walls. It was also found that the "two-wedge" deformation mode could be restricted if sufficiently long reinforcement was used. The study shows that it is rational to investigate the reinforcement load of reinforced soil walls subject to seismic loading without considering the previous long-term creep.

1. Introduction

Using backfill soils with cohesive fine contents to build geosynthetic-reinforced soil (GRS) retaining walls for permanent purposes has attracted considerable attention in recent years (e.g., Farrag et al., 2004; Benjamim et al., 2007). Such backfills are considered to be marginal since they contain cohesive fines that have a plasticity index (PI) >6 and may or may not exceed 15% (Elias et al., 2001). If justified, this practice can increase the cost-effectiveness of GRS walls. However, unlike clean granular soils, soils with cohesive fine contents generally exhibit distinctive creep response under constant loading, and GRS walls with such backfills have time-dependent responses that are very different from those using clean granular backfills (Allen and Bathurst, 2002; Liu et al., 2009; Yang et al., 2009). Another important issue is the seismic performance of this type of GRS walls. Case histories (e.g., Sandri, 1997; Ling et al., 2001) and extensive investigations (e.g., Ling et al., 2005a,b; El-Emam and Bathurst, 2007; Madhavi Latha and Murali Krishna, 2008, 2009; Huang and Wu, 2009; Sabermahani et al., 2009) have shown that GRS walls with granular backfill soils exhibit good performance under strong earthquake loading. However, since earthquakes generally occur during the service life of earth structures, the seismic performance of GRS walls using marginal backfills and having experienced years of creep remains a concern. In particular, it is necessary to clarify the reinforcement load and deformation mode of this type of GRS walls subject to seismic loading during service life, so that the seismic design can be soundly founded.

In most practices of seismic design (e.g., Elias et al., 2001), the reinforcement load is obtained by analysis of limit equilibrium. The reinforced soil wedge bounded by a Rankine's or Coulomb's failure surface is used together with a maximum seismic acceleration in the horizontal direction to calculate the reinforcement load. Maximum load in each reinforcement layer is assumed to occur at the failure surface. It is necessary to check the validity of these assumptions on GRS walls using marginal backfills and subject to seismic loading during service life. Regarding the deformation mode, shaking table tests, either in a 1 g or ng condition, have demonstrated that a "two-wedge" mode exists for most GRS walls with granular backfills under strong seismic loading (e.g., Matsuo

* Corresponding author. Tel.: +1 212 650 8007; fax: +1 212 650 6965.
E-mail address: hliu@ccny.cuny.edu (H. Liu).

0266-1144/$ – see front matter © 2010 Elsevier Ltd. All rights reserved.
doi:10.1016/j.geotexmem.2010.06.003

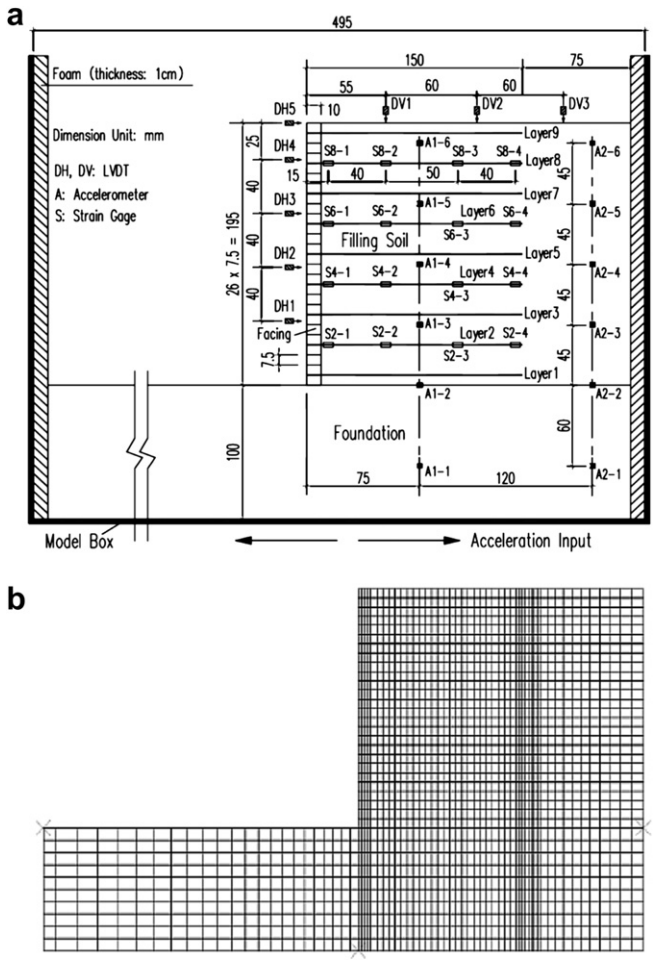

Fig. 1. Test setup and Finite Element mesh: (a) test setup (dimension in model scale); (b) Finite Element mesh.

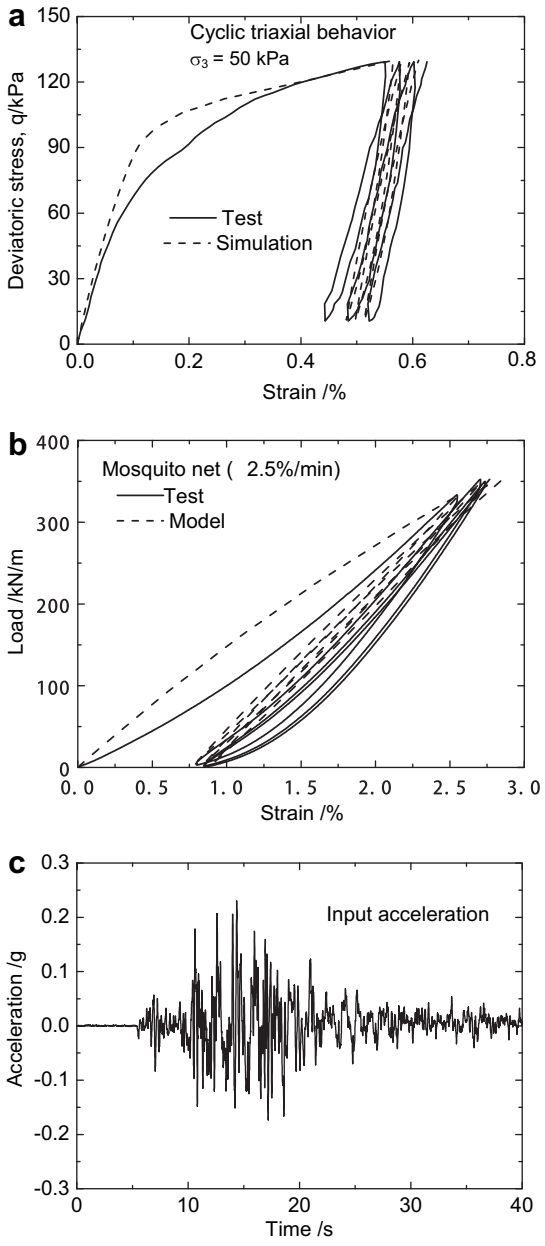

Fig. 2. Backfill soil, reinforcement, and input acceleration for the centrifuge model wall: (a) backfill soil; (b): mosquito net reinforcement in prototype scale; (c) input acceleration in prototype scale.

et al., 1998; Takahashi et al., 2001), but very limited study can be found on the deformation mode of GRS walls with marginal backfills subject to seismic loading after years of creep.

Calibrated Finite Element procedures are capable of reproducing the time-dependent responses of GRS structures under constant loading (e.g., Li and Rowe, 2008; Rowe and Skinner, 2001; Skinner and Rowe, 2003, 2005; Liu and Ling, 2007; Liu et al., 2009; Liu and Won, 2009). Their capacities in capturing the seismic responses of GRS walls have also been validated (e.g., Cai and Bathurst, 1995; Helwany et al., 2001; Ling et al., 2004, 2005a; Fakharian and Attar, 2007; Liu, 2009; Lee et al., 2010). In this study, a Finite Element procedure that is able to reproduce the long-term performance of GRS walls with marginal backfill soils (Liu et al., 2009) was extended for dynamic analysis and validated against a dynamic centrifuge test. The procedure was then used to investigate the reinforcement load and deformation mode of GRS walls subject to seismic loading after 5 years of creep. Model walls at

Table 1
Model parameters for backfill soils.

	G_0	K_0	R_f'	c/kPa	ϕ/°	ψ/°	k_1	K_2	a/s^{-1}	ξ/kPa^{-1}	m
Centrifuge backfill	750	620	0.85	0	36	6	1.50	1.05	0	_	_
Centrifuge foundation	550	460	0.85	25	27	_	1.60	1.25	_	_	_
Foundation soil	1250	1100	1.17	0	37	_	1.8	1.35	_	_	_
Soil i	550	500	0.9	16	30	0	1.65	1.25	3.5×10^{-6}	0.11	0.85
Soil ii	The same as Soil i								0	The same as Soil i	
Soil iii									1.0×10^{-6}		
Soil iv									1.0×10^{-5}		
Soil v									3.5×10^{-5}		

Table 2
Model parameters for geosynthetic reinforcements.

	J_e (kN/m)	A (kN/m)	$\bar{J}_p$ (kN/m)	h_0^b (kN/m)	c_1 (kN/m)	c_2 (kN/m)	n_0	κ	B (kN/m)	h_0^U (kN/m)	h_κ^L (kN/m)	η (kN/m)$^{1/n}$
Mosquito net	16,000	310	1100	8000	_	_	_	_	−55	4000	0	2.2×10^{25}
Grid A	1300	240	40	200	52	0.52	3.8	14	−45	1500	180	2.2×10^{9}
Grid B	The same as Case A											2.2×10^{8}
Grid C												2.2×10^{10}
Grid D												2.2×10^{11}
Grid E												2.2×10^{13}
Grid F												2.2×10^{25}
Grid G	270	The same as Case A										2.2×10^{25}
Grid H	550											2.2×10^{25}
Grid I	2170											2.2×10^{25}
Grid J	4350											2.2×10^{25}

a height of 8 m were used in the parametric study. The influences of various wall parameters on these two responses were studied.

2. Finite Element procedure

In this Finite Element procedure, the backfill soils were modeled using an elastoplastic–viscoplastic model obeying the Drucker–Prager yield criterion and Singh–Mitchell creep equation (Liu et al., 2009). In this model, the strain rate $\dot{\varepsilon}$of soil is assumed to consist of three components:

$$\dot{\varepsilon} = \dot{\varepsilon}_e + \dot{\varepsilon}_p + \dot{\varepsilon}_c \tag{1}$$

in which $\dot{\varepsilon}_e$, $\dot{\varepsilon}_p$, and $\dot{\varepsilon}_c$ are the elastic, plastic and creep strain rates, respectively. The Drucker–Prager Creep model (Abaqus Inc., 2004)

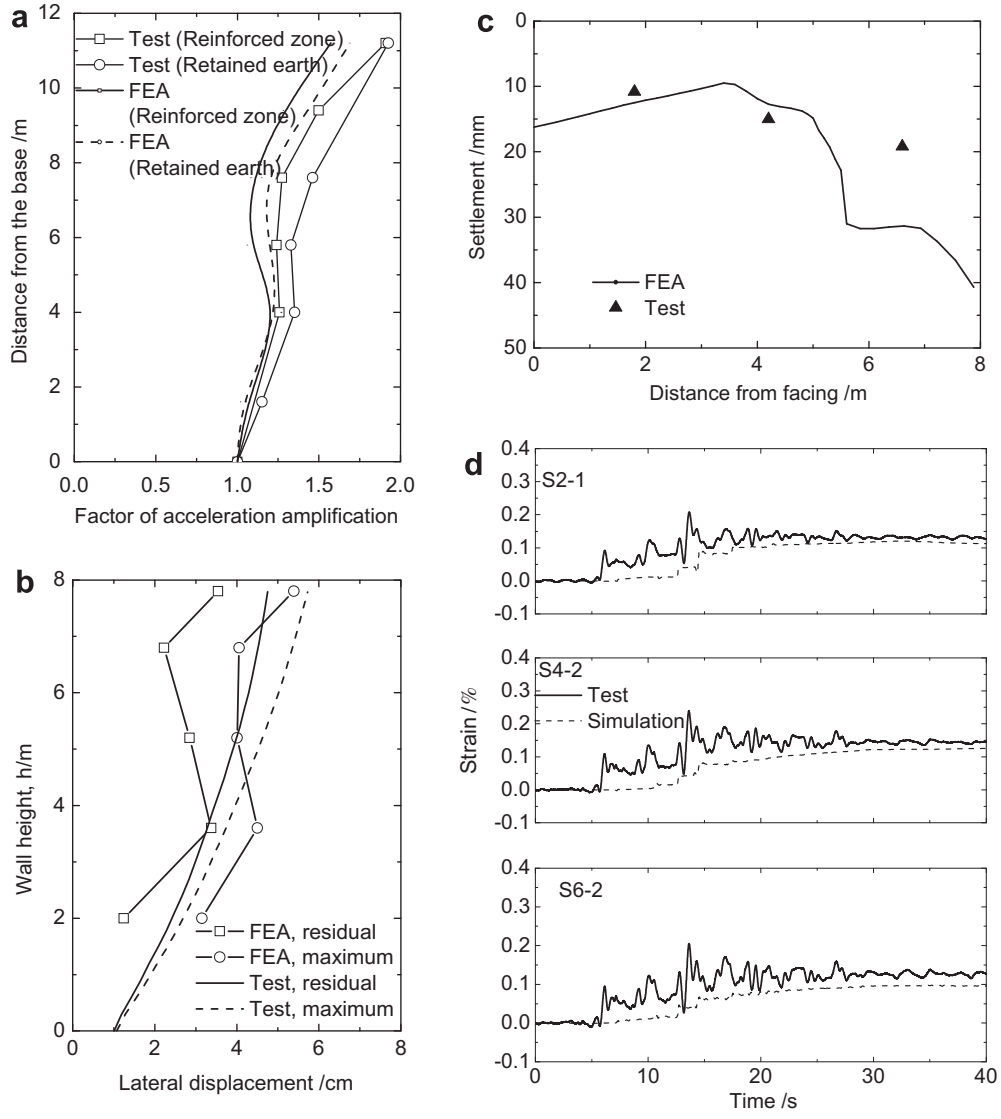

Fig. 3. Results of Finite Element simulation: (a) acceleration amplifications; (b) lateral facing displacements; (c) settlement of backfill surface at the end of shaking; (d) reinforcement strains at selected locations.

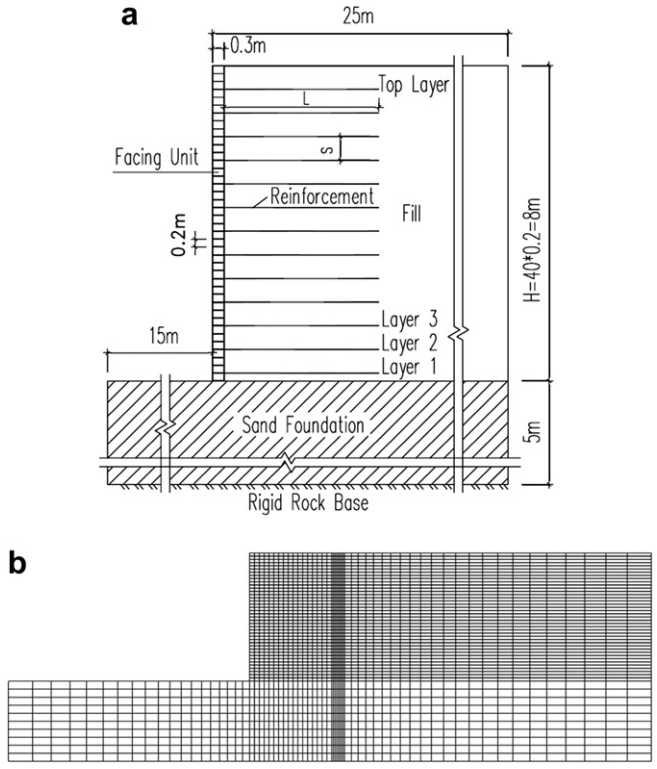

Fig. 4. Setup and Finite Element mesh of model reinforced soil walls.

was modified to take into account the nonlinear and cyclic hysteretic behaviors of soil before yielding. Under virgin-loading in general stress space, the tangent shear modulus G is defined as:

$$G = G_{\max}/\left(1 + R_f' G_{\max}|\gamma_{\text{oct}}^n|/\tau_{\text{oct}-f}\right)^2 \tag{2}$$

in which $G_{\max} = G_0 p_a (p/p_a)^{0.5}$, $\gamma_{\text{oct}}{}^n$ is the time-independent octahedral shear-strain, R_f' is the failure ratio, $\tau_{\text{oct}-f}$ is the yield octahedral shear-stress of soil, which is related to the shear strength of soil through cohesion c and internal angle of friction ϕ, p_a is the atmospheric pressure, p is the confining stress, and G_0 is a model parameter. The tangent shear-moduli in unloading and reloading, G_u and G_r, are defined respectively based on modified Masing rule as:

$$G_u = \frac{G_{\max}}{k_1\left(\left(1/k_1 + 0.5R_f' G_{\max}|\vec{\omega} - \vec{\omega}_u|\right)/\tau_{\text{oct}-f}\right)} \tag{3a}$$

$$G_r = \frac{G_{\max}}{k_2\left(1/k_2 + 0.5R_f' G_{\max}|\vec{\omega} - \vec{\omega}_r|\right)/\tau_{\text{oct}-f}} \tag{3b}$$

with k_1 and k_2 being two material constants to be calibrated from cyclic triaxial test. In Eq. (3), the unloading or reloading shear modulus is related to the "distance" from the point of unloading or reloading (Zhuang et al., 2007), with the vector $\vec{\omega}$ defined as:

$$\vec{\omega} = \frac{2}{\sqrt{3}}\left(e_{11}^n, e_{22}^n, e_{33}^n, \sqrt{2}e_{12}^n, \sqrt{2}e_{13}^n, \sqrt{2}e_{23}^n\right) \tag{4}$$

in which e_{ij}^n is the time-independent deviatoric strain tensor, $e_{ij}^n = \varepsilon_{ij}^n - (1/3)\varepsilon_{kk}^n\delta_{ij}$. $\vec{\omega}_u$ and $\vec{\omega}_r$ are the corresponding vectors at the points of unloading and reloading, respectively. The use of Eq. (4) and the concept of "distance" enable the model to be used in general stress space. It is noted that the "distance" $|\vec{\omega} - \vec{\omega}_u|$ or $|\vec{\omega} - \vec{\omega}_r|$ is equivalent to the difference in time-independent octahedral shear-strain $|\Delta\gamma_{\text{oct}}^n|$ under one-way cyclic loading.

The bulk modulus K of the soil is assumed to be dependent only on the confining stress:

$$K = K_0 p_a (p/p_a)^{0.5} \tag{5}$$

with the restriction that the Poisson's ratio μ must be $-1 < \mu < 0.5$. K_0 is another model parameter.

The yielding of soil is assumed to follow the Drucker–Prager Criterion. By using principal stresses and by defining the deviatoric stress $q = \sqrt{(1/2)[(\sigma_1 - \sigma_2)^2 + (\sigma_1 - \sigma_3)^2 + (\sigma_2 - \sigma_3)^2]}$ and the mean stress $p = (1/3)(\sigma_1 + \sigma_2 + \sigma_3)$, the Drucker–Prager yield surface can be written on p–q plane as:

$$f = q - p\tan\beta - d = 0 \tag{6}$$

in which β and d are related to the friction angle ϕ and cohesion c (Abaqus Inc., 2004), respectively. Non-associated flow rule is employed by using a dilation angle ψ different from the friction angle ϕ. In plane strain condition, the parameters β and d in Eq. (6) are related to the plane-strain strength and dilatancy parameters ϕ, c and ψ through the following relations (Abaqus Inc., 2004):

$$\sin\phi = \frac{\tan\beta\sqrt{3(9 - \tan^2\psi)}}{9 - \tan\beta\tan\psi} \quad c\cos\phi = \frac{\sqrt{3(9 - \tan^2\psi)}}{9 - \tan\beta\tan\psi}d \tag{7}$$

Only shear creep is considered in the constitutive model and the creep strain rate $\dot{\varepsilon}_c$ is described by the Singh–Mitchell creep equation (Singh and Mitchell, 1968):

$$\dot{\varepsilon}_c = a\cdot\exp(\xi\cdot\overline{\sigma}_c)\cdot(t_1/t)^m \tag{8}$$

in which $\overline{\sigma}_c = (q - p\tan\beta)/1 - (1/3)\cdot\tan\beta$, a, ξ, and m are three model parameters, and t_1 is the unit of time (1 min or 1 h, depending on the time unit used).

The proposed constitutive model is able to describe the salient features of soils under monotonic, cyclic, and sustained loadings. The model cannot describe the dependence of soil strength on stress path. But since plane strain condition was assumed in this study and the strength parameters of soil at plane strain conditions can be used in the analysis, the results of Finite Element Analysis can still reproduce the behavior of GRS retaining walls. Altogether 11 parameters are necessary to describe the cyclic, elastoplastic and creep behavior of soils, which are G_0, K_0, R_f, c, ϕ, ψ, a, ξ, k_1, k_2 and m. Direct-shear, plane strain, or triaxial-compression test can be used to obtain the strength and dilatancy parameters R_f', c,ϕ, and ψ of the soil; one triaxial creep test is needed to calibrate the creep parameters A, ξ and m; and at least one cyclic triaxial test is needed to calibrate the remaining nonlinear elastic and Masing rule parameters G_0, K_0 k_1 and k_2. For sandy soils, since their creep strain can generally be neglected, the creep parameters are not needed (by letting $a = 0$). The model was calibrated and validated against the element test results on different soils, which is reported in Wang et al. (2009).

Regarding other important components of a GRS earth retaining system, the geosynthetic reinforcements were modeled as 1-D bar elements using the elastoplastic viscoplastic bounding surface model for geosynthetics (Liu and Ling, 2005, 2007). This model can duplicate the nonlinearity, cyclic hysteresis (Bathurst and Cai, 1994; Ling et al., 1998; Jones and Clarke, 2007; Zanzinger et al. 2010), creep and stress relaxation (Leshchinsky et al., 1997; Yeo and

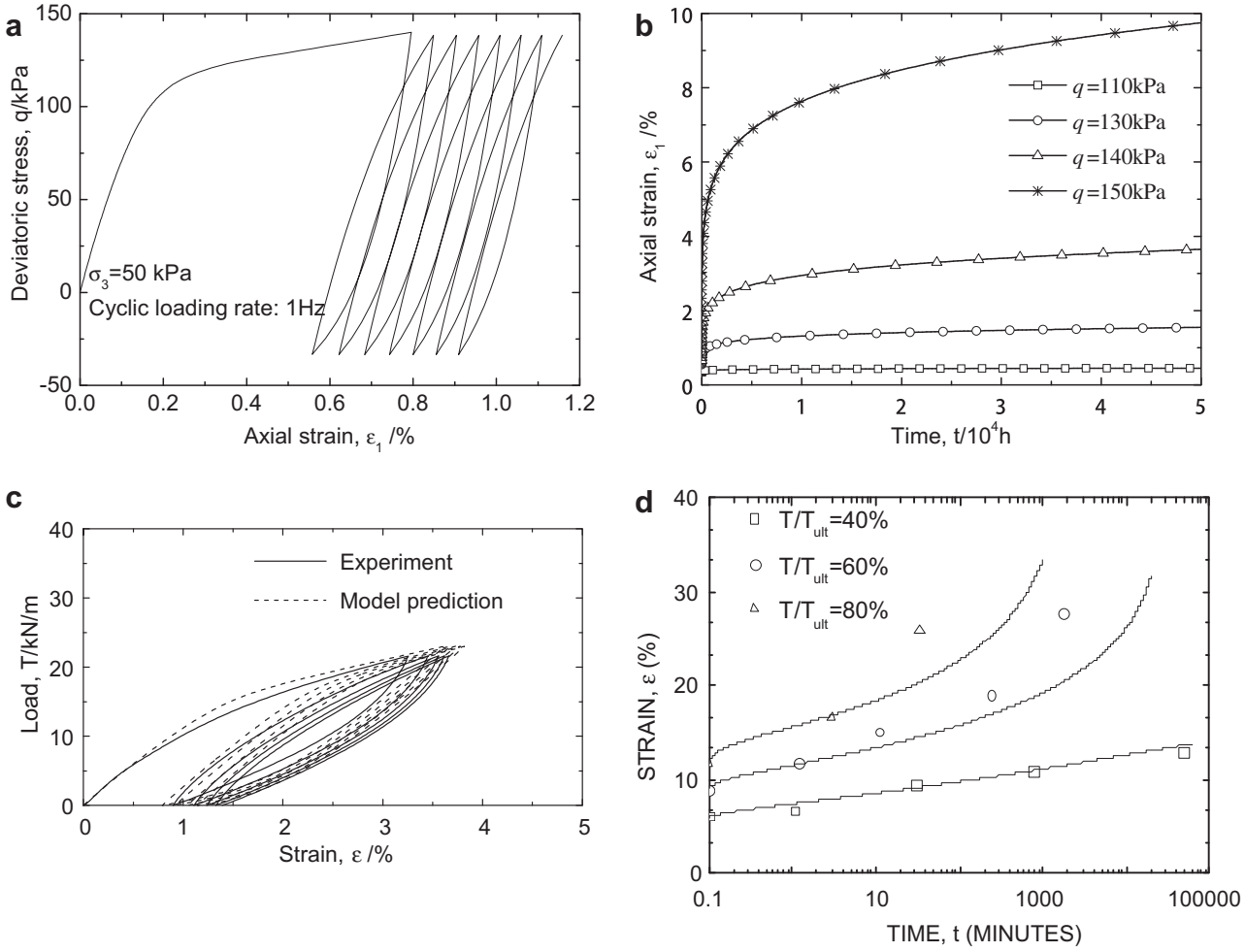

Fig. 5. Model soil, geogrid and earthquake excitation for the typical wall (a) cyclic response of model soil in triaxial compression ($\sigma_3 = 50$ kPa); (b) creep response of model soil in triaxial compression ($\sigma_3 = 50$ kPa); (c) cyclic response of geogrid ($\dot{\varepsilon} = 10\%$/min); (d) creep response of geogrid.

Hsuan, in press) of various geosynthetics with 12 parameters. Since it is not estimated that the reinforcement strain would be large enough to initiate tertiary creep (Hirakawa et al., 2003), the static curve in Liu and Ling (2005) was used in the present study. A brief introduction is given in Appendix I for reference purpose, and the detailed formulation can be found in Liu and Ling (2005, 2007). Thin-layer elements that follow Mohr–Coulomb failure criterion were used to simulate the soil-structure interface in the retaining wall system, and the facing elements were assumed to be linear elastic. The Finite Element Program ABAQUS 6.4 (Abaqus Inc., 2004), with the constitutive models for soil and geosynthetics incorporated, was used to conduct the long-term static analysis followed by dynamic analysis subject to horizontal seismic loading.

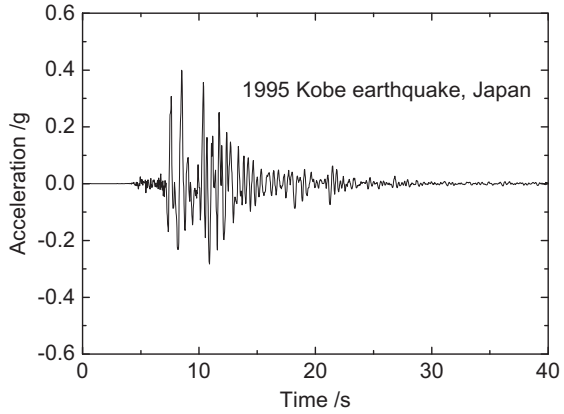

Fig. 6. Earthquake excitation.

The constitutive model for soil is able to capture the major damping of soil through the cyclic hysteresis. However, additional viscous damping of 5% was considered for soil in order to consider the fact that the constitutive model, like many others, cannot simulate properly the damping of soil when the strain level is small (Ling et al., 2005a). 5% viscous damping was also assigned to the facing and interface elements during dynamic analysis.

3. Validation of Finite Element procedure

The Finite Element procedure consists of two components: the long-term creep analysis and the following dynamic analysis. The first component was already validated in Liu et al. (2009), in which the long-term test on a clay-geotextile composite reported in Wu and Helwany (1996) was simulated with satisfactory results. Hence only the validation of the second component is reported herein.

It is difficult to conduct tests investigating the seismic response of GRS walls after long-term creep; and although field cases that had been in service for years before subject to seismic loading do exist, the detailed information required for numerical simulation, such as stress–strain relationship of materials as well as

Table 3
Summary of parametric study.

	Backfill soil	Reinforcement	Reinforcement length L	Reinforcement spacing D
Effects of soil creep (Case 1[a]–Case 5)	Soil i to Soil v	Grid A	$L = 0.7$H (5.6 m)	$D = 0.6$ m
Effects of reinforcement creep (Case 6–Case 10)	Soil i	Grid A to Grid F	$L = 0.7$H (5.6 m)	$D = 0.6$ m
Effects of reinforcement stiffness (Case 11–Case 14)	Soil i	Grid G to Grid J	$L = 0.7$H (5.6 m)	$D = 0.6$ m
Effects of reinforcement length (Case 15–Case 18)	Soil i	Grid A	$L = 0.5$H (3.5 m), $L = 0.6$H (4.2 m), $L = 0.8$H (6.4 m), $L = 1.0$H (8 m)	$D = 0.6$ m
Effects of reinforcement spacing (Case 19–Case 21)	Soil i	Grid A	$L = 0.7$H (5.6 m)	$D = 0.4$ m $D = 0.8$ m $D = 1.0$ m

[a] Case 1 is the base case.

quantitative responses after seismic loading were seldom documented. Therefore in this study a dynamic centrifuge test was carried out using the geotechnical centrifuge facility at Tsinghua University in order to validate the procedure's capacity in simulating the dynamic response of GRS retaining walls.

Under seismic loading, since the duration of loading is very short, the time-dependent responses of viscous materials, including cohesive soils and geosynthetic reinforcements, reflect as rate-dependent stiffness and hysteresis damping. According to many available studies (e.g., Cai and Bathurst, 1995; Helwany et al., 2001; Ling et al., 2004, 2005a; Liu, 2009), a sound numerical procedure for seismic numerical analysis must be able to properly describe the stiffness, damping, strength and dilatancy of materials as well as the dynamic geosynthetic-soil interaction. Therefore, in this study, the time-dependent responses before shaking were not considered in the centrifuge test and sandy soil was used as the backfill soil.

Fig. 1a shows the setup of the centrifuge test. A centrifugal force of 40 g was used. The height of the wall in prototype scale H was 7.8 m, with 9 layers of reinforcement (reinforcement spacing $D = 0.9$ m), each at a length of 5.6 m (in prototype scale, reinforcement length $L \approx 0.72$H). A medium-dense sandy soil that is commonly found in Beijing was used as the backfill soil, and a mosquito net was used as the reinforcement. A stiff clayey-silt was used as the foundation soil. The friction angle of the backfill soil ϕ was obtained from direct shear test as 36°. Aluminum blocks, the surfaces of which were purposely roughened, were used as facing units to simulate segmental facing, the dimension of which in prototype scale was 30 cm in height and 40 cm in width, respectively. Reinforcements were connected to the facing through friction between reinforcement and block. One component of the horizontal acceleration from the 1995 Kobe earthquake was scaled to a maximum acceleration of 0.24 g and used as the input at the base, as shown in Fig. 2c. The centrifuge model was instrumented with LVDT's, accelerometers and strain gages to measure the lateral facing displacement, backfill settlement, acceleration and reinforcement strain, as shown in Fig. 1a. Tensile tests on the mosquito net were conducted to obtain the correlation between strain gage reading and its real strain and the factor was used to interpret the reinforcement strain from the centrifuge test. The results of the centrifuge test can be found in Wang (2008).

The Finite Element simulation was conducted in the prototype scale. The model parameters for the backfill soil were calibrated using the soil strength and the result of a cyclic triaxial test. Since sandy soil can be assumed to be time-independent, the creep parameters a, ξ, and m are not needed. The model parameters are shown in Table 1 and the comparison of test result and model prediction is shown in Fig. 2a. The foundation soil was assumed to be nonlinear elastic, the behavior of which was described in Eqs. (2), (3a), (3b) and (5). The parameters are shown in Table 1, which were estimated from triaxial tests and the damping of low-plasticity cohesive soils (Vucetic and Dobry, 1991). The cyclic behavior of the mosquito net was converted into prototype scale by multiplying the original stiffness with 40 and simulated using the elastoplastic–viscoplastic bounding surface model (2005, 2007), but assuming it to be non-viscous, since negligible creep occurred during the test. The model parameters are shown in Table 2 and the comparison of test result and model prediction is shown in Fig. 2b. The interfaces in the reinforced soil model wall were simulated using thin-layer elements that followed Mohr–Coulomb failure criterion. The friction between backfill soil and mosquito net was obtained from direct shear test as $\delta = 30°$ $c = 0$, and those between reinforcement and block as well as block and block were estimated as $\delta = 35°$ and $c = 0$ from simple tilt table tests. The friction of the interface between facing block and backfill soil was estimated by using tan δ=(2/3) tan ϕ, in which ϕ is the friction angle of backfill soil. The facing blocks were assumed to be linear elastic following the parameters of ordinary aluminum, i.e. $E = 70{,}000$ MPa, $\mu = 0.32$ and $\gamma = 27$ kN/m^3.

Fig. 1b shows the Finite Element mesh. The initial stress state was obtained first using static analysis, the deformation and strain from which was reset to zero before dynamic analysis. Dynamic run was then carried out with the initial stress state. Fig. 3a shows the comparison of acceleration amplifications from centrifuge test and Finite Element analysis. The predicted accelerations were smaller than the experimental ones but the difference was not large. Fig. 3b shows the maximum lateral facing displacement during seismic excitation and that at the end of shaking, and Fig. 3c shows the settlement of backfill surface at the end of shaking, from which it can be seen that the Finite Element predictions were acceptable. The reinforcement strains at selected locations are shown in Fig. 3d. The Finite Element model reproduced satisfactorily the strain developments in the reinforcement during shaking.

The results of Finite Element simulations in this study show that the Finite Element procedure can reproduce the seismic response of GRS structures considering nonlinear material stiffness, hysteresis material damping, dynamic soil-structure interaction, and dilatancy and strength of soils. Together with that in Liu et al. (2009), the procedure can be used to simulate the response of reinforced soil retaining walls subject to seismic loading during service life.

4. Introduction of Finite Element parametric study

Using the validated procedure, Finite Element parametric study was conducted on geogrid-reinforced soil retaining walls at a height of 8 m. Concrete modular blocks at a height of 20 cm and a width of 30 cm were used as the facing units. Reinforcements were connected to facing units through friction with facing blocks. Fig. 4a shows the configuration of the model walls. A foundation of 5 m was considered, which was assumed to lay on rigid bed rock. The foundation soil was a medium-dense sandy soil, which was

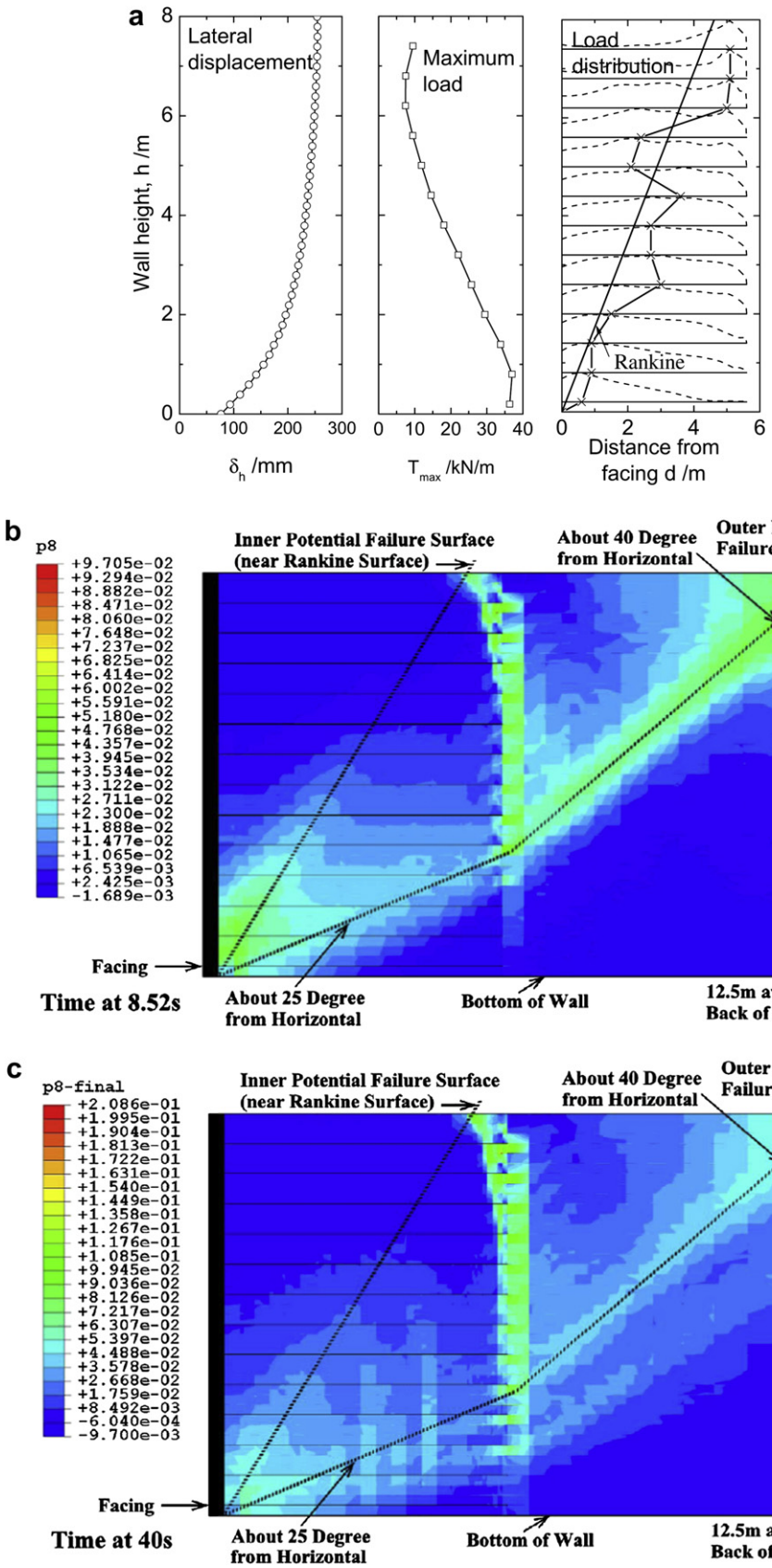

Fig. 7. Analyzing results of the typical wall: (a) lateral facing displacement, maximum reinforcement load and load distribution; (b) plastic shear strain at the moment of peak input acceleration; (c) plastic shear strain at the end of shaking.

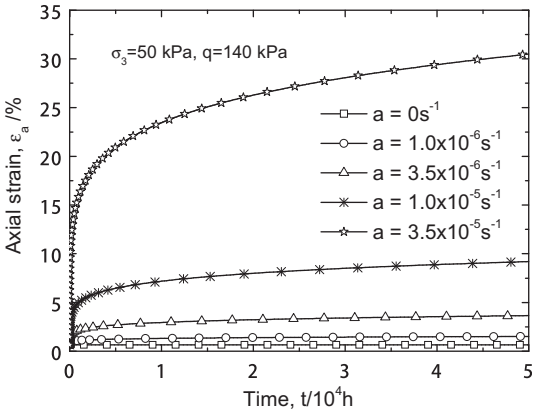

Fig. 8. Creep rates of backfill soil in triaxial compression.

assumed to be nonlinear elastic and described in Eqs. (2), (3a), (3b) and (5). The model parameters were calibrated from the tests in Sun and Shao (2005) and are shown in Table 1 (Wang, 2008). Large Finite Element mesh was used in the study, as shown in Fig. 4b for a wall with reinforcement length $L = 5.6$ m, and visco-elastic absorbing boundary (Abaqus Inc., 2004) was used at the sides to prevent wave reflection. Considering the large aperture size of geogrid, reinforcement and backfill soil were assumed to be perfectly bounded (Ling et al., 2005a). The strength between concrete blocks and that between geogrid and blocks were assumed to be $\delta = 35^\circ$ and $c = 0$, which remained the same in different analyses. The friction between facing block and backfill soil was obtained based on $\tan\delta = (2/3)\tan\phi$ and $c_{in} = (2/3)c$.

The deformation mode and reinforcement load of a typical reinforced soil wall using an HDPE geogrid as reinforcement at a length of 5.6 m ($L = 0.7$H) and a spacing of 0.6 m, subject to seismic loading after 5 years of creep, were firstly analyzed. A model cohesive backfill soil, the strength of which is $\phi = 30^\circ$ and $c = 16$ kPa, was used as the backfill. The model parameters are given in Table 1 (Soil i); and Fig. 5a and b shows the cyclic and creep responses of the model soil under triaxial compression. This cohesive model soil was used considering the cohesion of clayey-silt backfill due to unsaturation. The HDPE geogrid was a real one, the cyclic and creep responses of which are shown in Fig. 5c and d, respectively (Liu and Ling, 2005, 2007). The strength of the geogrid $T_{ult} = 55$ kN/m. The model parameters are shown in Table 2 (Grid A). A component of the 1995 Kobe earthquake, scaled to a maximum acceleration of 0.4 g, was used as the input excitation, as shown in Fig. 6.

Parametric study was then carried out to investigate the influences of various parameters of reinforced soil walls, including soil creep, reinforcement creep, reinforcement stiffness, reinforcement length and reinforcement spacing. In the parametric study, only the parameter of interest was varied, while the others were maintained to be the same as those of the typical wall. Table 3 summarizes the analyzed cases.

In the parametric study, simulation of construction was carried out first, followed by a creep analysis of 5 years. With the stress and strain states after 5 years of creep, the model walls were excited by the seismic loading. Only the results of seismic loading are presented in this paper. The results of creep analysis can be found in Liu et al. (2009).

5. Responses of a typical reinforced soil wall

The lateral facing displacement at the end of shaking, the maximum reinforcement load in each reinforcement layer, and the reinforcement load distribution are shown in Fig. 7a. The reinforcement load distribution gives the envelope of maximum load at each point. It can be seen that the maximum lateral displacement occurred approximately at the top of the wall, while the maximum reinforcement load occurred close to its base. The surface of maximum reinforcement load, which was obtained by connecting the points of maximum reinforcement load in each layer, was not the same as the Rankine's failure surface. It is closer to a Coulomb failure surface, which inclines at a smaller angle with the horizontal plane due to the consideration of facing friction.

Fig. 7b and c shows the distribution of octahedral plastic strain γ_{oct}^p at the moment of maximum excitation ($t = 8.52$ s) and that at the end of shaking, respectively. The two distributions were very similar in terms of areas of large strain. Although the plastic deformation seemed smeared at the lower wall portion, distinct trends can still be observed. It can be seen that under the input excitation (a component of 1995 Kobe earthquake scaled to $a_{max} = 0.4\,g$), a distinct failure surface did not fully develop in the reinforced soil zone, although at the lower portion of the wall, plastic deformation developed close to the Rankine's failure surface. On the other hand, a surface of large plastic deformation could be found in the lower portion of reinforced soil zone and extended into the retained earth, hereafter referred to as the "outer failure surface"; the third zone of large plastic deformation existed between the reinforced soil zone and retained earth, which is believed to be due to the different compressions of reinforced soil and retained earth. This deformation mode fits the "two-wedge failure" mode that was observed in model tests (e.g., Matsuo et al., 1998; Takahashi et al., 2001).

Observing the reinforcement load distribution and the deformation mode of the reinforced soil wall, it can be seen that the maximum loads in the lower reinforcement layers were the combined effect of the immature "internal failure surface" that was close to the Rankine's surface and that of the well-developed outer failure surface. It is therefore necessary to take into consideration the outer failure surface while calculating the maximum reinforcement loads subject to seismic loading, especially those in the lower reinforcement layers.

6. Effects of wall parameters

The effects of important wall parameters, including backfill creep, reinforcement creep, reinforcement stiffness, backfill strength, reinforcement length and reinforcement spacing, are discussed in this section.

6.1. Effects of backfill creep

The purpose of this series of analysis is to clarify the effects of backfill creep on the reinforcement load and deformation mode of reinforced soil walls subject to seismic loading during service life. The model parameter a in Eq. (8) was varied to simulate the change of soil creep, which is shown in Fig. 8.

Fig. 9a shows the maximum reinforcement loads in different layers and the corresponding load distributions. Backfill creep had negligible influence on the overall reinforcement load due to both static and seismic loadings. In Liu et al. (2009), it was shown that the creep of backfill soil influenced considerably the reinforcement load under constant static loading. Larger backfill creep led to larger reinforcement load after 5 years of creep. This effect was compensated under seismic loading, which can be explained by the isotach response of viscous soil under cyclic loading (Tatsuoka et al., 1999). It has been observed in experiments that viscous soil exhibits stiffer response in the subsequent loading after creep, tending to merge with the stress–strain curve under virgin

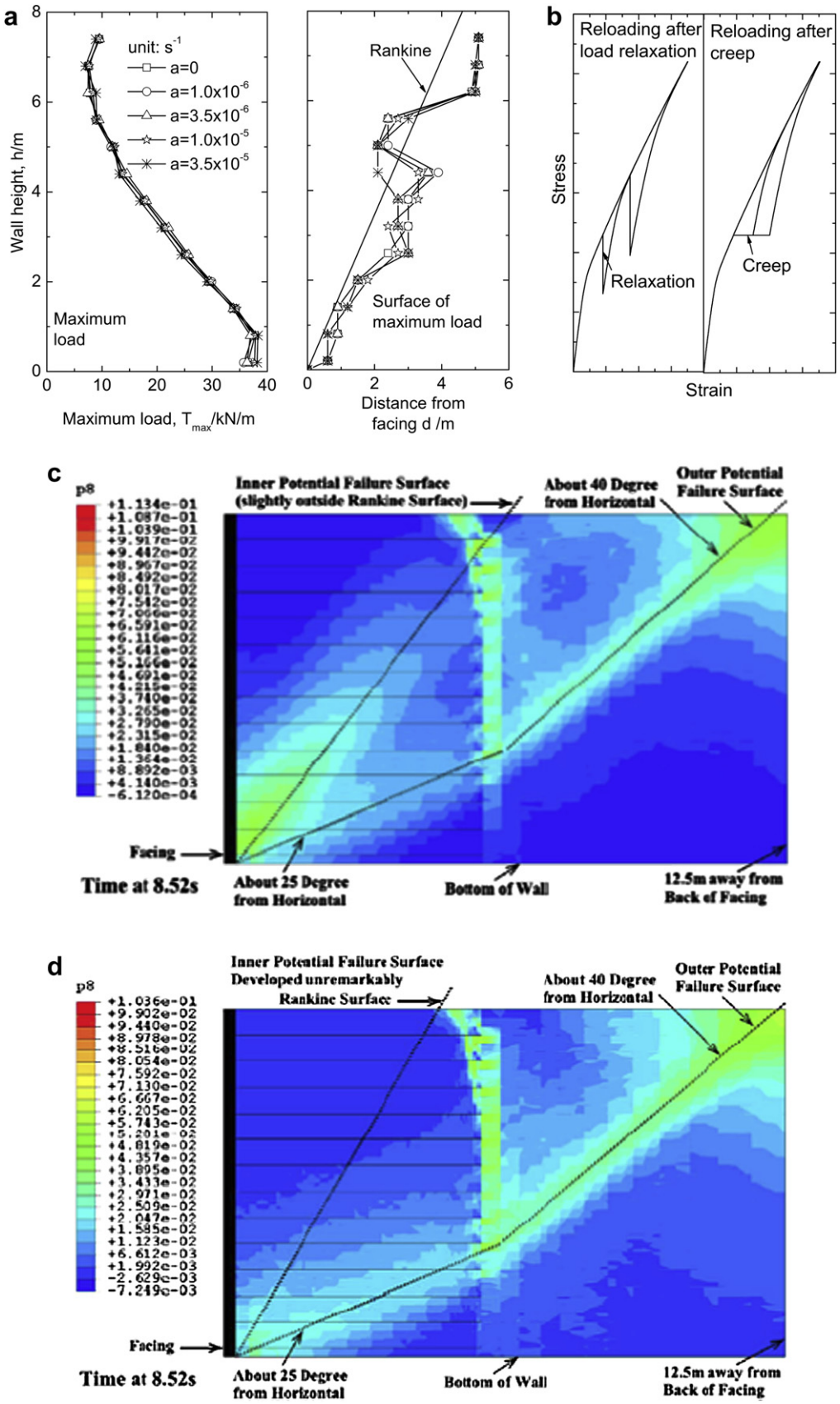

Fig. 9. Effects of soil creep rate: (a) maximum reinforcement load and load distribution; (b) illustration of isotach response of viscous materials; (c) plastic shear strain at the moment of peak input acceleration for non-viscous backfill; (d) plastic shear strain at the moment of peak input acceleration with $a = 3.5 \times 0^{-5}\ s^{-1}$.

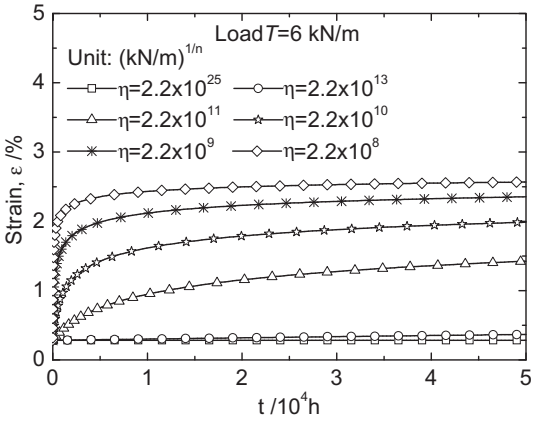

Fig. 10. Creep responses of gensynthetic reinforcements under a constant tension of 6 kN/m.

loading, as illustrated in Fig. 9b. Thus under the same seismic loading, backfill soil with larger time-dependent response demonstrated larger stiffness due to larger creep deformation before seismic loading, which led to smaller load increment in the reinforcement. This smaller load increment, superimposing the larger static load after 5 years of creep, resulted in similar reinforcement load with that if the backfill soil was less viscous.

The creep rate of backfill soil did not influence the development of outer failure surface but it influenced the development of internal failure surface in reinforced soil walls, as shown in Fig. 9c and d. With non-viscous backfill soil, the potential internal failure surface developed distinctively close to the Rankine's surface, but it could hardly be seen if the creep of backfill soil was very large. This is basically due to the load distribution between backfill and reinforcement under constant static loading (Liu et al., 2009). More static load was carried by the backfill soil when its creep rate was smaller than that of the reinforcement. It should be pointed out that the overall lateral facing-displacements after seismic loading were quite different with different backfill creeps, although the results are not given herein due to space restriction. The one with large creep of backfill soil showed considerably larger lateral displacement, which was due to the creep deformation before seismic loading (Liu et al., 2009).

6.2. Effects of reinforcement creep

The parameter η in Eq. (I.8) in Appendix I was varied to simulate the creep rates of different reinforcements, as shown in Fig. 10. Fig. 11a shows the maximum reinforcement loads and the corresponding load distributions. With the same backfill soil, an increase in the creep rate of reinforcement slightly decreased the maximum reinforcement load, and shifted the surface of maximum reinforcement load to some extent. The small difference in maximum reinforcement load was the combined effects of lower reinforcement load with larger reinforcement creep in comparison to that of backfill under constant static loading (Liu et al., 2009), and the corresponding larger load increment under seismic loading due to isotach response of geosynthetic reinforcement (Hirakawa et al., 2003).

Similar to the effects of backfill creep, reinforcement creep influenced significantly the development of potential internal failure surface, but had very small effects on the outer one, as shown in Fig. 11b and c. Almost identical outer failure surfaces were observed in all the cases with different creep rates of reinforcement. The potential internal failure surface was more obvious with larger reinforcement creep, which was also mainly due to the load distribution between soil and reinforcement under constant static loading. Larger creep rate of reinforcement rendered more load to be carried by backfill soil, which led to a more distinct potential internal failure surface (Liu et al., 2009). This surface further developed under seismic loading. On the other hand, with smaller reinforcement creep, reinforcement carried more load under static loading, and even with seismic loading, the plastic deformation of the reinforced soil did not develop extensively, as shown in Fig. 11b.

6.3. Effects of reinforcement stiffness

In this series of analysis, reinforcement was assumed to be non-viscous by setting the parameter η to be a very large value. The purpose is to decouple the effects of η on reinforcement stiffness under dynamic loading, since as shown in Liu and Won (2009), under the same loading rate, increasing η results in an increase in the reinforcement stiffness. The initial stiffness J_0 was varied to simulate different reinforcement stiffnesses.

An increase in reinforcement stiffness significantly increased reinforcement load and considerably altered the deformation mode. As can be seen in Fig. 12a, maximum reinforcement load increased with an increase in the reinforcement stiffness, and the surface of maximum reinforcement load shifted towards the facing units. The same trend was observed in Liu (2009), in which cohesionless soil was used as backfill soil.

Regarding deformation mode, with smaller reinforcement stiffness, the outer failure surface moved upward and towards the facing units, as shown in Fig. 12b and c. Larger reinforcement stiffness could restrict the shear deformation in the lower portion of reinforced zone, which further influenced the development of failure surface in the retained earth.

It can be seen from these results that it may be necessary to consider the effects of reinforcement stiffness in designing reinforced soil wall against seismic loading. However, it is difficult to take it into account with analysis of limit equilibrium (e.g., Fakher and Jones, 2008), which has been routinely used in practice.

Also by comparing the results of this section and last section, the effects of reinforcement creep and reinforcement stiffness can be unified to certain extent. An increase in the reinforcement creep is similar to a decrease in the reinforcement stiffness under the same loading rate (Kaliakin et al., 2000), and hence they have similar effects on reinforcement load, although with different magnitudes. The influences on deformation mode could not be clearly witnessed under different creep rates of reinforcement in this study, which might be explained by the fact that the change of rate-dependent stiffness was not very large.

6.4. Effects of reinforcement length and spacing

The effect of reinforcement length on maximum reinforcement load was small when the length was not long enough to restrict the development of the outer failure surface, as shown in Fig. 13a. However, when the reinforcement length was sufficiently long, the loads in the upper reinforcement layers increased considerably, although those in the lower layers decreased. The increase of reinforcement load in these layers was due to the fact that they restricted the development of the outer failure surface, as seen in Fig. 13c. With sufficiently long reinforcement, the plastic shear deformation smeared in the reinforced soil zone and an outer failure surface could not be witnessed. Before that, reinforcement length influenced the location of outer failure surface, but not the inclined angles, as can be seen in Figs. 7b and 13b.

Maximum reinforcement load increased linearly with an increase in the reinforcement spacing, which is not shown herein

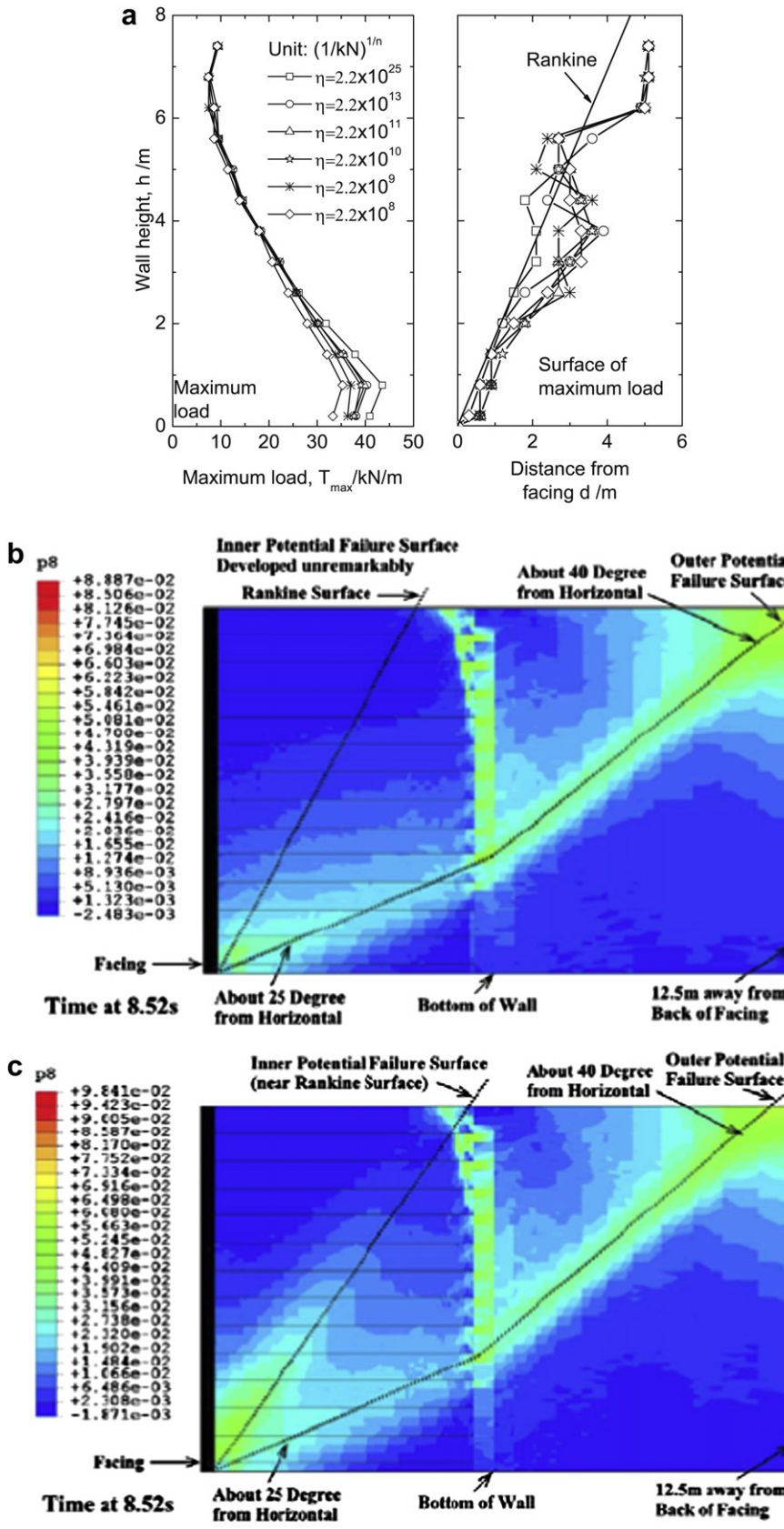

Fig. 11. Effects of reinforcement creep rate: (a) maximum reinforcement load and load distribution; (b) plastic shear strain at the moment of peak input acceleration for non-viscous reinforcement; (c) plastic shear strain at the moment of peak input acceleration with $\eta = 2.2 \times 0^8$ $(1/\mathrm{kN})^{1/n}$

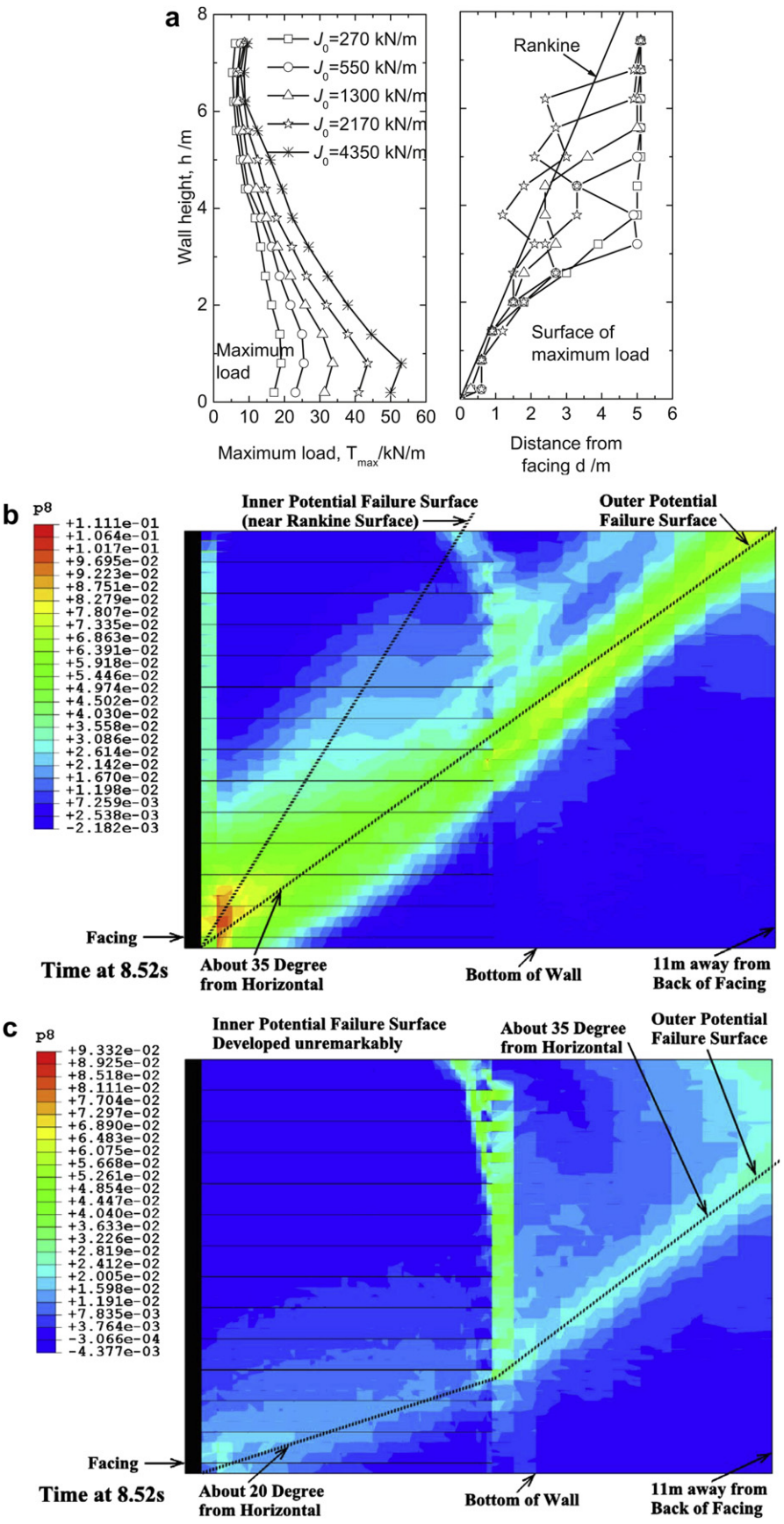

Fig. 12. Effects of reinforcement stiffness: (a) maximum reinforcement load and load distribution; (b) plastic shear strain at the moment of peak input acceleration when $J_0 = 270$ kN/m; (c) plastic shear strain at the moment of peak input acceleration when $J_0 = 4350$ kN/m.

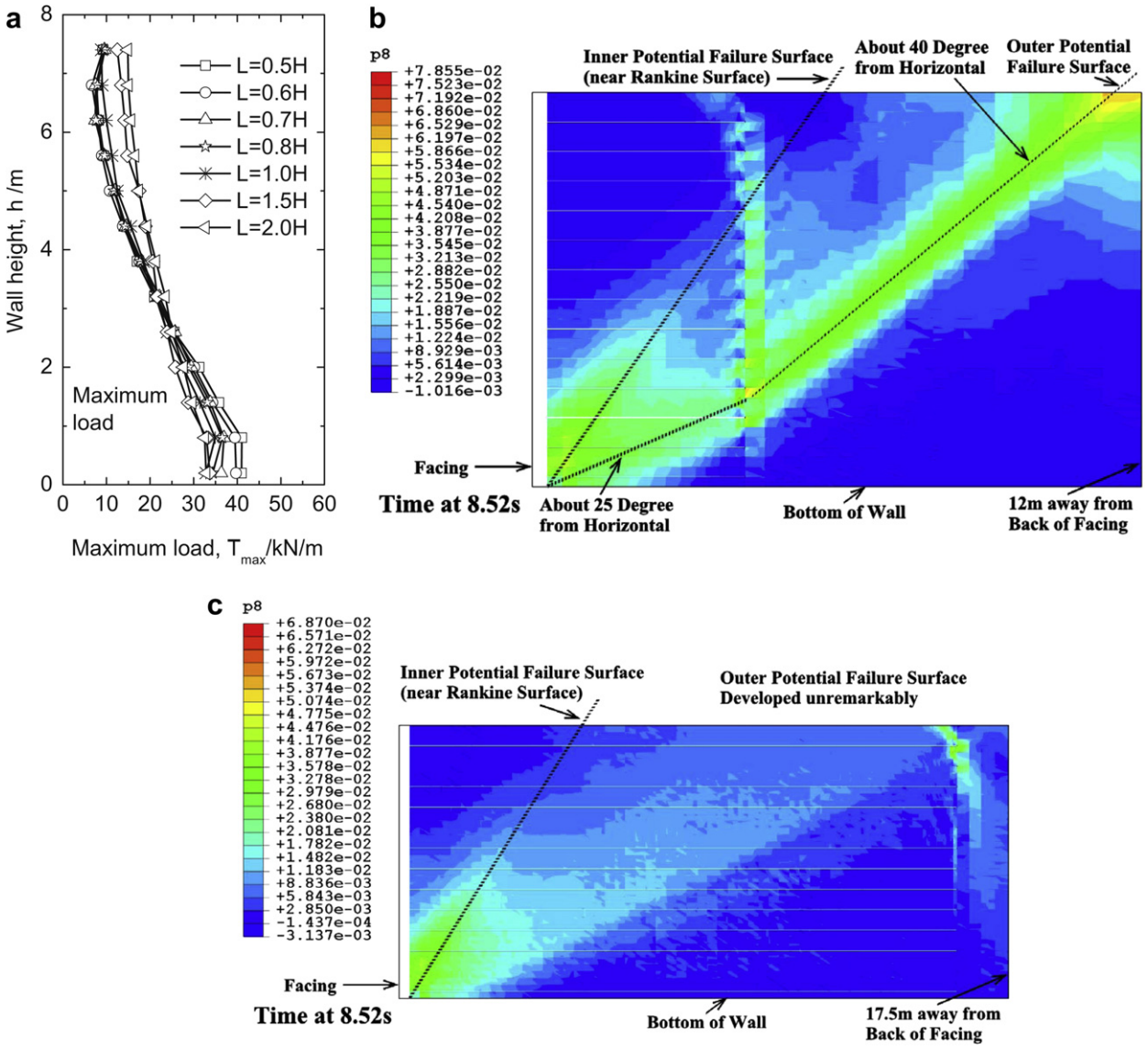

Fig. 13. Effects of reinforcement length: (a) maximum reinforcement load; (b) plastic shear strain at the moment of peak input acceleration with $L = 0.5H$; (c) plastic shear strain at the moment of peak input acceleration with $L = 2.0H$.

due to space restriction. It seems that the viscous properties of backfill soil and reinforcement do not change such a trend, although the slope may be different (Ling et al., 2005a; Liu, 2009). Regarding the (potential) failure surfaces, the internal one developed more distinctively with larger reinforcement spacing, while the outer one moved slightly upward and towards the facing with an increase in the reinforcement spacing, as shown in Fig. 14.

7. Discussion and conclusions

Finite Element method was used to investigate the deformation mode and reinforcement load of reinforced-soil walls with marginal backfill subject to seismic loading after 5 years of creep. Model walls at a height of 8 m were analyzed. The Finite Element procedure consists of two steps. The first step simulates the creep response of reinforced soil walls under constant static loading, and the second one analyzes the seismic response, using the stress and strain states at the end of creep analysis as initial states. The capacity of the procedure to simulate the long-term response of reinforced soil walls was validated in Liu et al. (2009); while its capacity to reproduce seismic response was validated against a dynamic centrifuge test conducted at Tsinghua University.

It was found from the study that under strong seismic loading, reinforced soil walls exhibited a distinctive “two-wedge” deformation mode. A well-developed failure surface extended from the lower portion of reinforced soil zone into the retained earth, referred to as “outer failure surface” in this paper; another well-developed failure surface existed between the reinforced-soil zone and the retained earth, which is believed to come from the different compressions of reinforced soil and retained earth. Inside the reinforced soil zone, an internal failure surface close to the Rankine’s surface generally did not develop extensively under seismic loading of 0.4 g, the extent of which depended on the soil and reinforcement parameters. Corresponding to this deformation mode, the maximum reinforcement load in each reinforcement layer was the combined effects of the outer failure surface and the potential internal failure surface.

For general backfill soils and geosynthetic reinforcements that may be used in practice, their creep rates have small effects on the

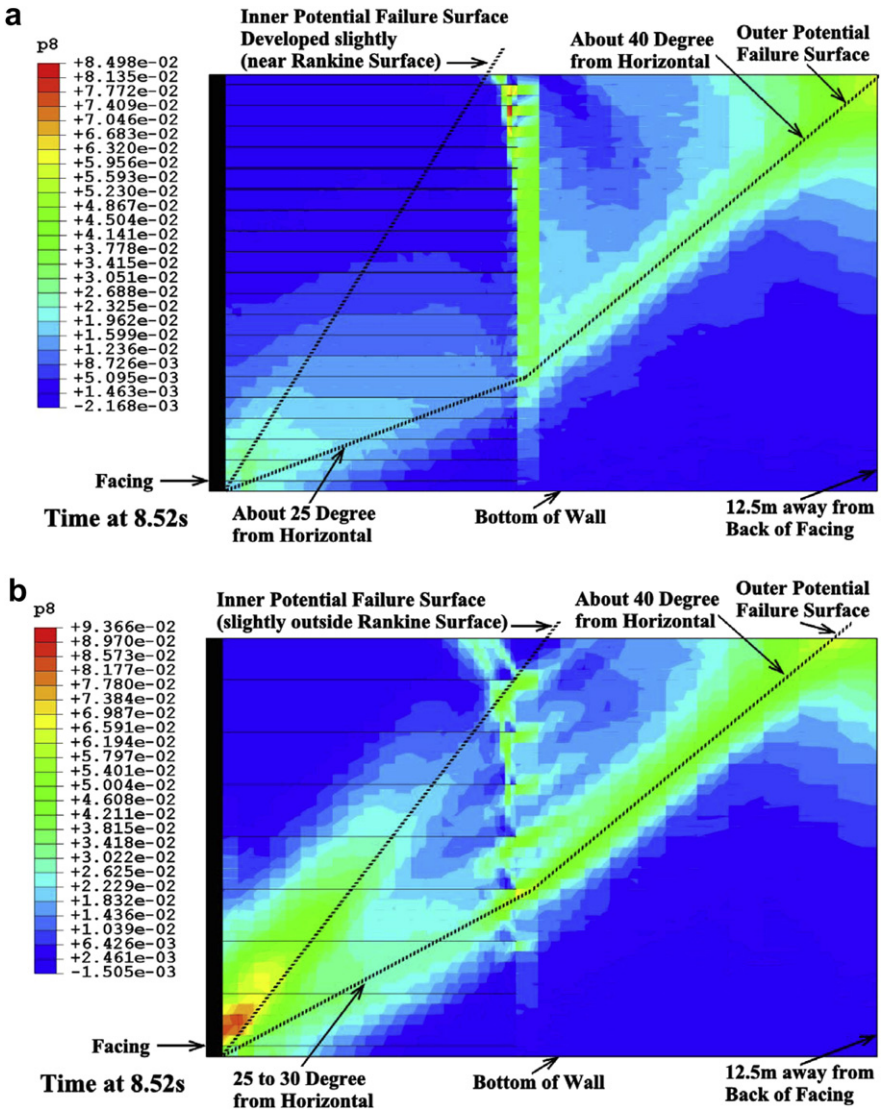

Fig. 14. Effects of reinforcement spacing: (a) plastic shear strain at the moment of peak input acceleration with $d = 0.4$ m; (b) plastic shear strain at the moment of peak input acceleration with $d = 1.0$ m.

reinforcement load of reinforced soil walls subject to seismic loading after 5 years of creep, which was due to the isotach responses of viscous materials. Among these two factors, the influence of reinforcement creep is slightly larger. Reinforcement stiffness influenced considerably the reinforcement load. With an increase in the reinforcement stiffness, reinforcement load increased significantly, and the small change of reinforcement load due to the change of reinforcement creep can also be explained by the difference in rate-dependent stiffness. Reinforcement load increased linearly with reinforcement spacing, regardless of the different viscous properties of backfill and reinforcement. Reinforcement length had only negligible influences when the length was not long enough to restrict the development of the outer failure surface; but the loads in the upper reinforcement layers increased considerably when their lengths are sufficiently long.

Creep rates of backfill soil and reinforcement also had small influence on the developments of the outer failure surface in the range investigated, but they influenced the development of the (potential) internal failure surface that was close to the Rankine's surface. The latter was mainly due to the load redistribution among backfill and reinforcement under constant static loading before the seismic event (Liu et al., 2009). Reinforcement stiffness had evident influences on the development of the outer failure surface, which cannot be captured by analysis of limit equilibrium. Reinforcement spacing and reinforcement length also affected the locations of the outer failure surface as well as the development of (potential) internal failure surface. In particular, when reinforcement length was sufficiently long, the outer failure surface did not develop; the plastic strain was smeared in the reinforced soil zone. This result could be meaningful for seismic design of reinforced soil walls.

The results of this study indicate that it is rational to investigate the reinforcement load of reinforced soil walls subject to seismic loading without considering the previous long-term creep, but how to consider the effects of reinforcement stiffness in the analysis of limit equilibrium, which is the common practice at present, still deserves further investigation.

The Finite Element procedure used in this study was validated separately against model tests for its capacities in simulating long-term creep and seismic response of GRS walls. It might be more rational to calibrate it using experiments that test the long-term creep followed by seismic response of GRS walls, but is not so possible at present.

Appendix I

The constitutive model for geosynthetics is based on bounding surface plasticity and overstress viscoplasticity, in which the total strain rate is assumed to be composed of the following three components:

$$\dot{\varepsilon} = \dot{\varepsilon}^{e} + \dot{\varepsilon}^{p} + \dot{\varepsilon}^{vp} \tag{I.1}$$

where $\dot{\varepsilon}^{e}$, $\dot{\varepsilon}^{p}$, and $\dot{\varepsilon}^{vp}$ are the elastic, plastic and viscoplastic strain rates, respectively. In Liu and Ling (2007), two types of geosynthetics, Type A and Type B, were distinguished, but only Type A geosynthetics were used in this study.

The elastic strain rate $\dot{\varepsilon}^{e}$ is obtained by $\dot{\varepsilon}^{e} = \dot{T}/J_0$. Bounding surface plasticity is used to describe the elastoplastic behavior of the elastoplastic–viscoplastic model. The bounding lines on the tension and compression sides are defined as

$$T_{+} = A + \bar{J}_{p}\varepsilon^{p}, \quad T_{+} = B + \bar{J}_{p}\varepsilon^{p} \tag{I.2}$$

in which A and B are the intercepts of the two bounding lines with the load axis (T-axis), respectively, and $\bar{J}_{p}$ is the slope of the bounding lines. T_{+} and T_{-} are the bounding loads per unit width on the tension and compression sides, respectively. The hardening parameters are expressed as

$$h^{VL} = h_0^{L}, \quad h^{RL} = h_0^{L} + h_k^{L}\sqrt{\varepsilon_{p}}, \quad h^{U} = h_0^{U} \tag{I.3}$$

where h_0^{L}, h_k^{L}, and h_0^{U} are model parameters, with superscripts VL, U, and RL indicating virgin loading, unloading, and reloading, respectively.

The plastic stiffness of the model is defined using Eqs. (I.2) and (I.3) as

$$J_{p} = \frac{dT}{d\varepsilon^{p}} = \bar{J}_{p} + h\frac{\delta}{\delta_{in} - \delta} \tag{I.4}$$

with δ being the distance of the present stress state to the bounding line and δ_{in} being the initial distance at the beginning of loading path.

The viscoplastic behavior is described using the Perzyna formulation. Since it is estimated that tertiary creep would not occur in the reinforcements for the problems investigated, the static curve introduced for Type A geosynthetics in Liu and Ling (2007) is used for monotonic loading in this study

$$T_{s} = c_1\varepsilon^{c_2} \tag{I.5}$$

Upon unloading, the static curve is expressed as:

$$T_{s} = T_0 + 2c_1[|\varepsilon - \varepsilon_0|/2]^{c_2} \tag{I.6}$$

and upon reloading,

$$T_{s} = T_0 - 2c_1[|\varepsilon - \varepsilon_0|/2]^{c_2} \tag{I.7}$$

where T_0 and ε_0 are the load and strain at the start of unloading or reloading. With these static curves, the viscoplastic strain rate is defined as

$$\dot{\varepsilon}^{vp} = \frac{1}{\eta}|T - T_{s}|^{n}\mathrm{sign}(\dot{\varepsilon}), \quad T \geq T_{s} \tag{I.8}$$

where η is the viscous coefficient, $n = n_0[1 + \exp(-\kappa\varepsilon^{vp})]$, and n_0 and κ are two material constants.

Altogether 12 model parameters are needed to describe cyclic, creep and stress relaxation behavior of Type A geosynthetic reinforcements, which are J_0, A, $\bar{J}_p$, h_0^{L}, B, h_0^{U}, h_k^{L}, c_1, c_2, n_0, κ, and η.

References

Abaqus Inc., 2004. ABAQUS/Standard User's Manuals, Version 6.4. Rhode Island, Providence.

Allen, T.M., Bathurst, R.J., 2002. Observed long-term performance of geosynthetic walls, and implications for design. Geosynthetics International 9 (5–6), 567–606.

Bathurst, R.J., Cai, Z., 1994. In-isolation cyclic load-extension behavior of two geogrids. Geosynthetics International 1 (1), 1–19.

Benjamim, C.V.S., Bueno, B.S., Zornberg, J.G., 2007. Field monitoring evaluation of geotextile-reinforced soil-retaining walls. Geosynthetics International 14 (2), 100–118.

Cai, Z., Bathurst, R.J., 1995. Seismic response analysis of geosynthetic reinforced soil segmental retaining walls by Finite Element method. Computers and Geotechnics 17 (4), 523–546.

El-Emam, M.M., Bathurst, R.J., 2007. Influence of reinforcement parameters on the seismic response of reduced-scale reinforced soil retaining walls. Geotextiles and Geomembranes 25 (1), 33–49.

Elias, V., Christopher, B.R., Berg, R.R., 2001. Mechanically Stabilized Earth Walls and Reinforced Soil Slopes Design and Construction Guidelines. Report FHWANHI-00-043. Federal Highway Administration (FHWA), Washington, DC.

Fakher, H.N.A., Jones, C.J.F.P., 2008. Evaluating the effects of the magnitude and amplification of pseudo-static acceleration on reinforced soil slopes and walls using the limit equilibrium Horizontal Slices Method. Geotextiles and Geomembranes 26 (3), 263–278.

Farrag, K., Abu-Farsakh, M., Morvant, M., 2004. Stress and strain monitoring of reinforced soil test wall. Transportation Research Record 1868, 89–99.

Fakharian, K., Attar, I.H., 2007. Static and seismic numerical modeling of geosynthetic-reinforced soil segmental bridge abutments. Geosynthetics International 14 (4), 228–243.

Helwany, S.M.B., Budhu, M., McCallen, D., 2001. Seismic analysis of segmental retaining walls I: model verification. Journal of Geotechnical and Geoenvironmental Engineering ASCE 127 (9), 741–749.

Hirakawa, D., Kongkitkul, W., Tatsuoka, F., Uchimura, T., 2003. Time dependent stress–strain behaviour due to viscous properties of geogrid reinforcement. Geosynthetics International 10 (6), 176–199.

Huang, C.C., Wu, H.J., 2009. Seismic displacement analysis of a reinforced soil model wall considering progressive development of reinforcement force. Geosynthetics International 16 (3), 222–234.

Jones, C.J.F.P., Clarke, D., 2007. The residual strength of geosynthetic reinforcement subjected to accelerated creep testing and simulated seismic events. Geotextiles and Geomembranes 25 (3), 155–169.

Kaliakin, V.N., Dechasakulsom, M., Leshchinsky, D., 2000. Investigation of the isochrone concept for predicting relaxation of geogrids. Geosynthetics International 7 (2), 79–99.

Lee, K.Z.Z., Chang, N.Y., Ko, H.Y., 2010. Numerical simulation of geosynthetic-reinforced soil walls under seismic shaking. Geotextiles and Geomenbranes 28 (4), 317–334.

Leshchinsky, D., Dechasakulsom, M., Kaliakin, V.N., Ling, H.I., 1997. Creep and stress relaxation of geogrids. Geosynthetics International 4 (5), 463–479.

Li, A.L., Rowe, R.K., 2008. Effects of viscous behaviour of geosynthetic reinforcement and foundation soils on embankment performance. Geotextiles and Geomembranes 26 (4), 317–334.

Ling, H.I., Mohri, Y., Kawabata, T., 1998. Tensile properties of geogrids under cyclic loadings. Journal of Geotechnical and Geoenvironmental Engineering, ASCE 124 (8), 782–787.

Ling, H.I., Leshchinsky, D., Chou, N.N.S., 2001. Post-earthquake investigation on several geosynthetic-reinforced soil retaining walls and slopes during 1999 Ji-Ji Earthquake of Taiwan. Soil Dynamics and Earthquake Engineering 21 (4), 297–313.

Ling, H.I., Liu, H., Kaliakin, V., Leshchinsky, D., 2004. Analyzing dynamic behavior of geosynthetic-reinforced soil retaining walls. Journal of Engineering Mechanics ASCE 130 (8), 911–920.

Ling, H.I., Liu, H., Mohri, Y., 2005a. Parametric study on the behavior of reinforced soil retaining walls under earthquake loading. Journal of Engineering Mechanics ASCE 131 (10), 1056–1065.

Ling, H.I., Mohri, Y., Leshchinsky, D., Burke, C., Matsushima, K., Liu, H., 2005b. Large-scale shaking table tests on modular-block reinforced soil retaining walls. Journal of Geotechnical and Geoenvironmental Engineering ASCE 131 (4), 465–476.

Liu, H., Ling, H.I., 2005. Constitutive modeling of the time-dependent monotonic and cyclic behavior of geosynthetics. In: Ling, H.I. (Ed.), Geosynthetics and Geosynthetic-engineered Soil Structures. Columbia University, New York, NY, pp. 281–302.

Liu, H., Ling, H.I., 2007. A unified elastoplastic–viscoplastic bounding surface model of geosynthetics and its applications to GRS-RW analysis. Journal of Engineering Mechanics ASCE, 801–815.

Liu, H., Wang, X., Song, E., 2009. Long-term behavior of GRS retaining walls with marginal backfill soils. Geotextiles and Geomembranes 27 (4), 295–307.

Liu, H., Won, M.S., 2009. Long-term reinforcement load of geosynthetic-reinforced soil retaining walls. Journal of Geotechnical and Geoenvironmental Engineering ASCE 135 (7), 875–889.

Liu, H., 2009. Analyzing the reinforcement loads of geosynthetic-reinforced soil walls subject to seismic loading during the service life. Journal of Performance of Constructed Facilities ASCE 23 (5), 292–302.

Madhavi Latha, G., Murali Krishna, A., 2008. Seismic response of reinforced soil retaining wall models: influence of backfill relative density. Geotextiles and Geomembranes 26 (4), 335–349.

Murali Krishna, A., Madhavi Latha, G., 2009. Seismic behaviour of rigid-faced reinforced soil retaining wall models: reinforcement effect. Geosynthetics International 16 (5), 364–373.
Matsuo, O., Tsutsumi, T., Yokoyama, K., Saito, Y., 1998. Shaking table tests and analyses of geosynthetic-reinforced soil retaining walls. Geosynthetics International 5 (1–2), 97–126.
Rowe, R.K., Skinner, G.D., 2001. Numerical analysis of geosynthetic reinforced retaining wall constructed on a layered soil foundation. Geotextiles and Geomembranes 19 (7), 387–412.
Sabermahani, M., Ghalandarzadeh, A., Fakher, A., 2009. Experimental study on seismic deformation modes of reinforced-soil walls. Geotextiles and Geomembranes 27 (2), 121–136.
Sandri, D., 1997. A performance summary of reinforced soil structures in the greater Los Angeles area after the Northridge earthquake. Geotextiles and Geomembranes 15 (4–6), 235–293.
Singh, A., Mitchell, J.K., 1968. General stress–strain–time function for soils. Journal of the Soil Mechanics and Foundations Division, ASCE 94 (SM1), 21–46.
Sun, Y., Shao, L., 2005. Experimental study on deformation behaviors of sandy soil under triaxial cyclic loading. Chinese Journal of Geotechnical Engineering 27 (11), 1353–1357 (in Chinese with English abstract).
Skinner, G.D., Rowe, R.K., 2003. Design and behaviour of geosynthetic reinforced soil walls constructed on yielding foundations. Geosynthetics International 10 (6), 200–214.
Skinner, G.D., Rowe, R.K., 2005. Design and behaviour of a geosynthetic reinforced retaining wall and bridge abutment on a yielding foundation. Geotextiles and Geomembranes 23 (3), 235–260.
Takahashi, A., Takemura, J., Shimodaira, T., 2001. Seismic performance of reinforced earth wall with geogrid. In: Proceedings 15th ICSMGE, pp. 1265–1268. Istanbul, Turkey.
Tatsuoka, F., Santucci de Magistris, F., Momoya, M., Maruyama, N., 1999. Isotach behaviour of geomaterials and its modelling. In: Proceedings of the 2nd International Conference on Pre-Failure Deformation Characteristics of Geomaterials, pp. 491–499. Torino, Italy.
Vucetic, M., Dobry, R., 1991. Effects of soil plasticity on cyclic response. Journal of Geotechnical Engineering ASCE 117 (1), 89–107.
Wang, X., 2008. Investigating the seismic behavior of GRS walls after long-term creep. PhD thesis, Tsinghua University, Beijing, China.
Wang, X., Liu, H., Song, E., 2009. A practical elasto-plastic visco-plastic model for soils. Journal of Hohai University 37 (2), 166–170 (in Chinese with English abstract).
Wu, J.T.H., Helwany, S.M.B., 1996. A performance test for assessment of long-term creep behavior of soil-geosynthetic composites. Geosynthetics International 3 (1), 107–124.
Yang, G., Zhang, B., Lv, P., Zhou, Q., 2009. Behaviour of geogrid reinforced soil retaining wall with concrete-rigid facing. Geotextiles and Geomembranes 27 (5), 350–356.
Yeo, S.S., Hsuan, Y.G. Evaluation of creep behavior of high density polyethylene and polyethylene–terephthalate geogrids. Geotextiles and Geomembranes, in press. doi:10.1016/j.geotexmem.2009.12.003.
Zanzinger, H, Hangen, H, Alexiew, D., 2010. Fatigue behaviour of a PET-Geogrid under cyclic loading. Geotextiles and Geomembranes 28 (3), 251–261.
Zhuang, H., Chen, G., Liang, Y., Xu, M., 2007. A developed dynamic viscoelastic constitutive relation of soil and implemented by ABAQUS software. Rock and Soil Mechanics 28 (3), 436–442 (in Chinese with English abstract).